JOURNAL OF THE AMERICAN CHEMICAL SOCIETY

pubs.acs.org/JACS

Article

Unraveling the Steric Effect of Trialkyl Phosphates on the Solvation Sheath and Solid Electrolyte Interphase in High-Efficiency Magnesium Electrolytes

Chang Li, Rohith Srinivaas Mohanakrishnan, Jinghan Li, Rishabh D. Guha, Kristin A. Persson, and Linda F. Nazar*

Cite This: *J. Am. Chem. Soc.* 2026, 148, 4087−4096

Read Online

ACCESS | Metrics & More | Article Recommendations | Supporting Information

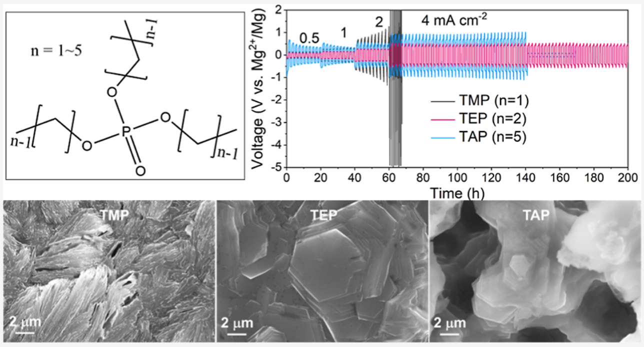

ABSTRACT: Designing Mg-compatible and chloride-free electrolytes is important to achieving high-voltage and long-life Mg metal batteries. In electrolytes based on $Mg(OTf)_2$/diglyme: triethyl phosphate that exhibit near 100% Coulombic efficiency for Mg plating/stripping at high current densities and capacities, the TXP (X = alkyl group) plays a key role. Herein, we unveil steric hindrance as the fundamental origin of this role in optimizing the Mg^{2+} solvation structure and forming electrolyte-derived solid electrolyte interphases. The steric hindrance was tuned by systematically changing the alkyl chain length of the phosphate (TXP) from one to five. Its impact on altering bulk electrolyte solvation and interfacial SEI chemistry was studied by combining both spectroscopy techniques and theoretical modeling methods. We demonstrate that low steric hindrance leads to easy decomposition of phosphate solvents, whereas high steric hindrance fails to interrupt Mg^{2+}-triflate/diglyme interactions. TEP with medium hindrance shows optimized behavior in both scenarios, which is the origin of its superior electrochemical performance. Our finding provides a new solvent design principle at the molecular level for chloride-free Mg^{2+} electrolytes.

■ INTRODUCTION

High-voltage rechargeable magnesium batteries are a promising candidate for "beyond lithium-ion battery" technologies.[1−4] Their merits originate from the use of magnesium metal anodes that have higher earth abundance, lower cost, and better safety relative to lithium metal anodes.[5] The bottleneck of implementing magnesium anodes in these batteries is developing a suitable electrolyte, which ideally is noncorrosive, inexpensive, and anodically stable at high voltages (>3.5 V vs Mg^{2+}/Mg) and can sustain efficient magnesium electrodeposition/stripping (E/S).[2,6]

Classic chloride-based electrolytes have been studied for decades owing to their high efficiency of magnesium E/S; however, they suffer from high corrosivity to battery components and are now challenged by the newly designed chloride-free carborane/organoborate-based electrolytes.[7] These electrolytes not only exhibit comparable magnesium anode efficiency to that of chloride-based electrolytes but also show high anodic stability (~4 V vs Mg^{2+}/Mg) and good compatibility with various cathode materials.[8−10] No significant corrosivity to common metals (for example, stainless steel) is observed in these electrolytes, yet their expensive synthesis/purification procedures plague their wide applications.[11−13]

To tackle these issues, various solvent/additive engineering strategies have been applied to electrolytes with conventional and commercially available salts, including magnesium bis(trifluoromethanesulfonimide) ($Mg(TFSI)_2$) and trifluoromethanesulfonate ($Mg(OTf)_2$). These electrolytes historically suffer from the strong ion pairing effect.[14,15] Traditionally, the carbonate-based solvents used in lithium- or sodium-ion batteries tend to readily decompose on the surface of magnesium and passivate it. Ether-type organic liquids were thus regarded as the only choice for the solvents for magnesium−ion electrolytes,[13] although they suffer from minor decomposition during the magnesium E/S.[6,10,12] However, typical ether solvents [for example, dimethoxyethane (DME) and diglyme (G2)] are not adequately polarizable to interrupt conventional Mg^{2+}−$TFSI^-$/OTf^- ion pairs, which induces easy anion decomposition[14] and aggravates solvent

Received: August 30, 2025
Revised: January 8, 2026
Accepted: January 9, 2026
Published: January 20, 2026

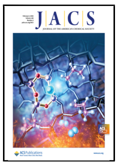

https://doi.org/10.1021/jacs.5c14645

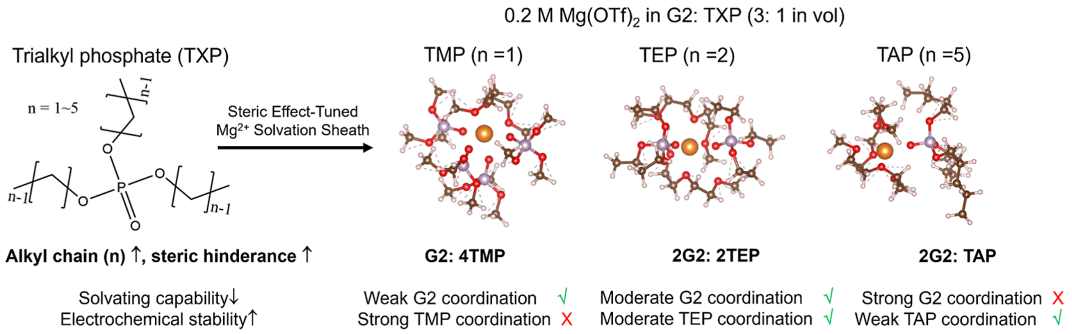

Figure 1. Schematic illustration of the effect of the alkyl chain length on steric hindrance in the Mg^{2+} solvation sheath (from MD simulations) and the electrochemical stability of solvents.

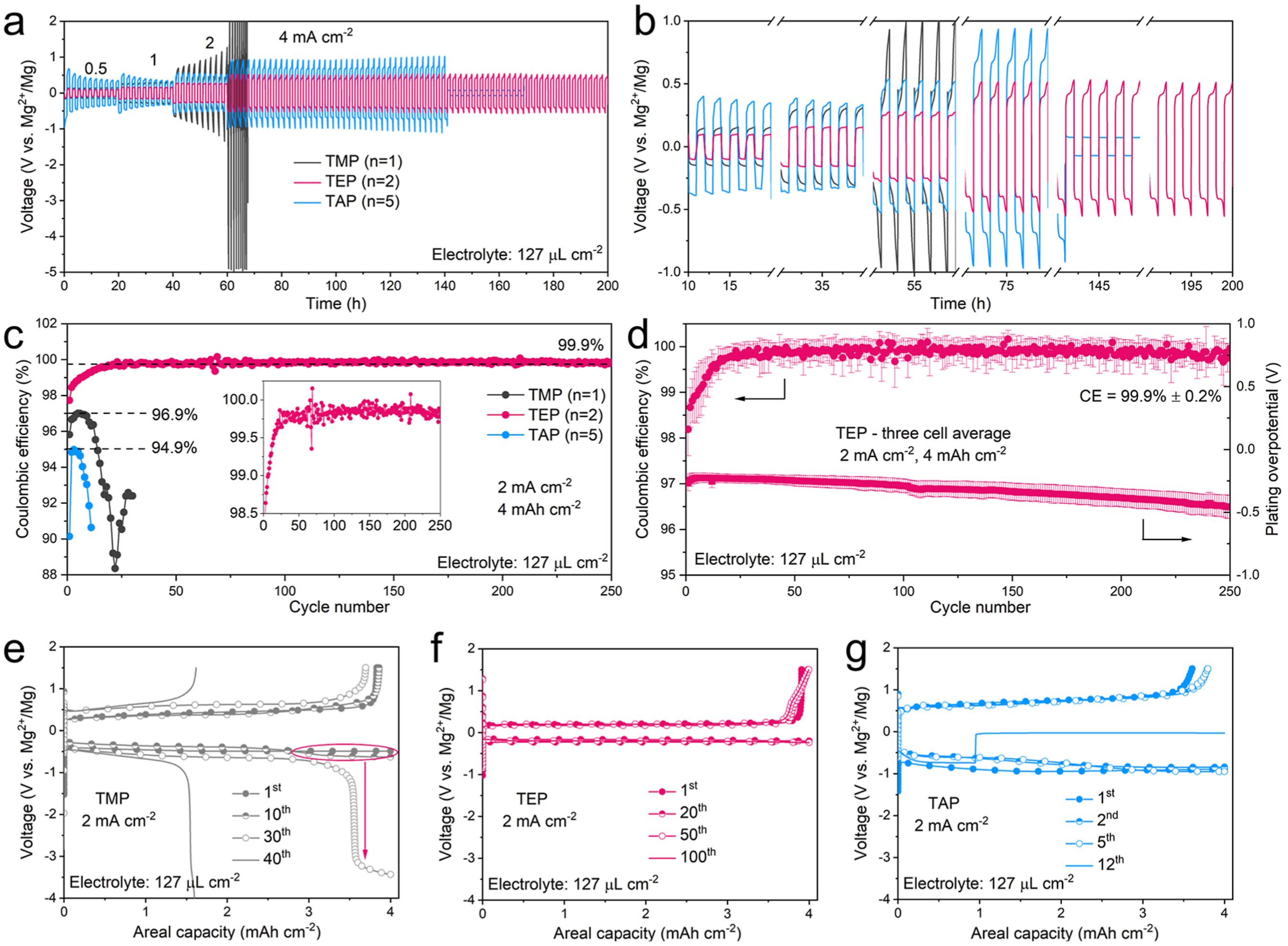

Figure 2. Electrochemistry of magnesium electrodeposition/stripping in various electrolytes. (a) Voltage profiles of Mg||Mg symmetric cells at different current densities and (b) the magnified view of the initial 200 h. Each plating or stripping process lasted for 1 h. All cells were preactivated at 0.1 mA cm^{-2} (0.1 mAh cm^{-2}). (c) The evolution of Coulombic efficiency as a function of cycle numbers in Mg||Cu asymmetric cells at 2 mA cm^{-2} (4 mAh cm^{-2}) in various electrolytes. (d) The evolution of average Coulombic efficiency and end-point plating overpotentials in TEP-based electrolyte based on three independent cells. (e–g) The corresponding voltage profiles in 0.2 M $Mg(OTf)_2$ with (e) G2: TMP, (f) G2: TEP, and (g) G2: TAP.

degradation.[15] Wang et al. reported a methoxyethylamine solvent as a chelant to strongly solvate with Mg^{2+}, simultaneously limiting the side reactions of both anions and DME solvents during the magnesium electrodeposition.[6] The addition of methoxyethylamine in conventional ether solvents leads to high Coulombic efficiency (CE) at 98–99.5% of magnesium E/S for both $Mg(TFSI)_2$ and $Mg(OTf)_2$-based electrolytes at controlled conditions (<0.5 mA cm^{-2} and <0.5 mAh cm^{-2}).[6,16,17] Very recently, we reported a highly efficient electrolyte — 0.2 M $Mg(OTf)_2$/diglyme (G2): triethyl phosphate (TEP, 3:1 in vol)[18] — that achieves near 100% CE at practical conditions with current densities ranging from 2–5 mA cm^{-2} and areal capacities of 4–10 mAh cm^{-2} during long-term cycling. TEP has been considered as a strongly polar

https://doi.org/10.1021/jacs.5c14645
J. Am. Chem. Soc. 2026, 148, 4087–4096

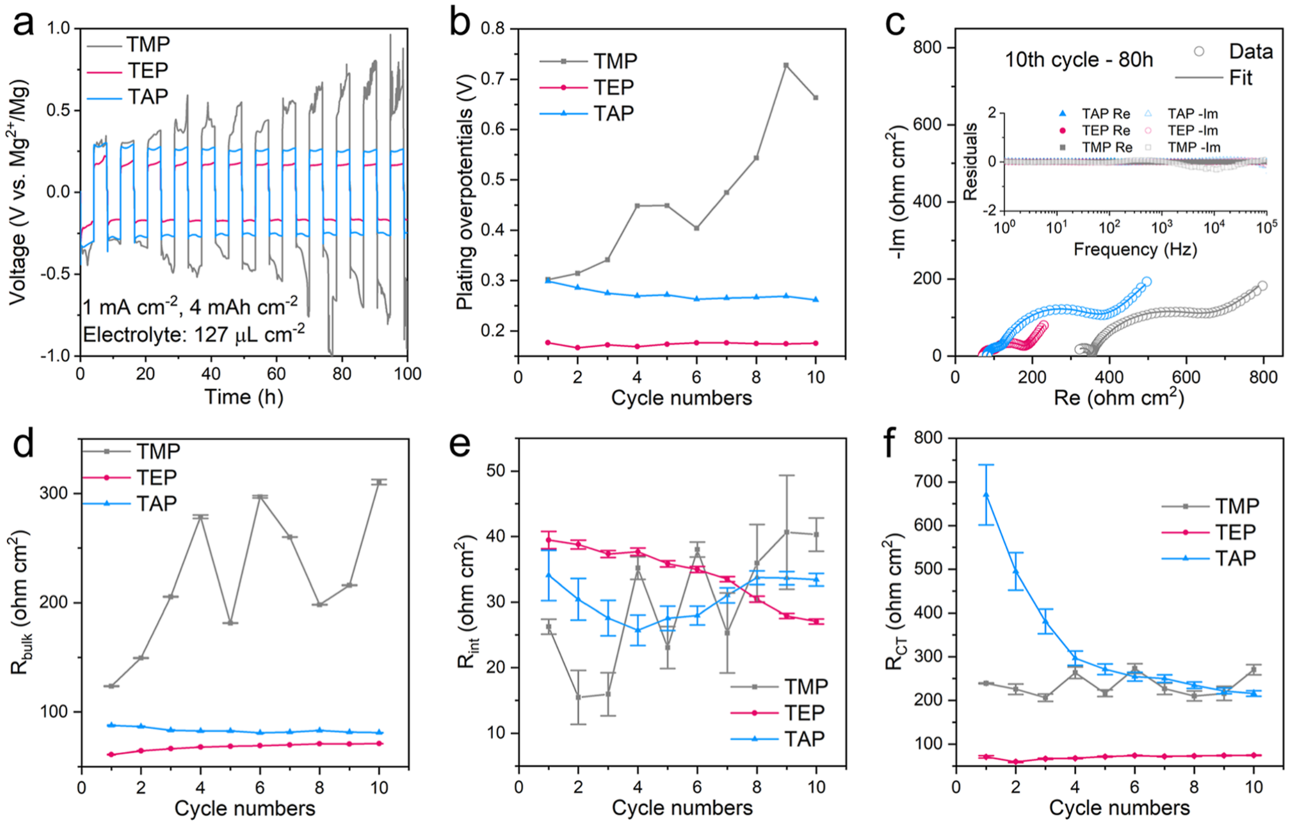

Figure 3. Impedance studies of magnesium electrodeposition/stripping in various electrolytes. (a) The voltage profiles of Mg||Mg symmetric cells at 1 mA cm^{-2} (4 mAh cm^{-2}). All cells were precycled at 0.1 mA cm^{-2} (0.1 mAh cm^{-2}). (b) The corresponding plating overpotentials for the initial 10 cycles (80 h). (c) The representative fitted Nyquist plots at the 10th cycle (inset shows the fitting residuals). (d) Fitted bulk ionic resistance (R_{bulk}), (e) interphase resistance (R_{int}), and (f) charge transfer resistance (R_{CT}) with fitting error as a function of cycle number.

solvent to interrupt the Mg^{2+}−OTf^{-} contact ion pairs (CIPs) and increase solubility, which suppresses the decomposition of anions during magnesium electrodeposition. However, the origin of its impact on boosting desolvation kinetics and its robustness against electrochemical reduction during magnesium plating need further scrutiny.

Herein, we systematically investigated the effect of alkyl chain lengths in trialkyl phosphate solvents on tuning the magnesium E/S electrochemistry. Steric hindrance is unveiled as a key descriptor in tuning the solvation sheath in bulk electrolytes and the solid electrolyte interphases (SEIs) formed on magnesium anode surfaces. We reported two vital aspects of steric hindrance in these electrolytes (Figure 1). First, the solvating capability of these phosphates decreases with the increase of alkyl chain lengths, leading to weaker dissociation of the Mg^{2+}−G2 interaction that causes easy G2 degradation during Mg plating. Second, the phosphates are less stable against decomposition with shorter alkyl chains, where the trimethyl phosphate (TMP) with only one methyl group shows the poorest stability and continuous consumption during the long-term cycling. These difference in electrolyte stability leads to very distinctive SEIs on the Mg surface and Mg deposition morphologies. Molecular dynamics (MD) simulations and density functional theory (DFT) calculations reveal that the steric hindrance resulting from different alkyl chain lengths in these trialkyl phosphates plays a vital role in tuning Mg^{2+} solvation structure and the decomposition preference of various electrolyte species. Our study highlights the importance of small solvent molecule variance as tiny as one single alkyl group in determining the electrolyte stability and electrochemistry of metal plating/stripping.

RESULTS AND DISCUSSION

Electrochemistry of Magnesium Electrodeposition/Stripping

Magnesium E/S chemistry was examined in symmetric cells with 0.2 M $Mg(OTf)_2$/G2/TXP (3:1 in vol), where TXP is a trialkyl phosphate with a formula of $(CH_3)(CH_2)_{n-1}PO_4$ [TMP (n = 1), TEP (n = 2), TPP (n = 3), TBP (n = 4), TAP (n = 5)]. We note that $Mg(OTf)_2$ can barely dissolve in G2 itself but dissolves in the G2-TXP cosolvents. The concentration of salt and volume ratio of solvents were based on our previous study.[18] The TMP electrolyte showed a low magnesium E/S overpotential of 135 mV at 0.5 mA cm^{-2}, yet dramatically increased overpotentials of up to 1 V were evident at 2 mA cm^{-2} (Figure 2a,b and S1). Applying a higher current density of 4 mA cm^{-2} induced the immediate cell failure with a polarization over 10 V. In contrast, the TEP electrolyte exhibited the lowest overpotentials of 96, 155, 252, and 395 mV at current densities of 0.5, 1, 2, and 4 mA cm^{-2}, respectively. With TAP, the overpotential was double that of TEP, and the cell quickly shorted after 140 h at 4 mA cm^{-2}, in contrast to the stable cycling of TEP for over 900 h (Figure S2). The CE of the asymmetric Mg||Cu cell using the TEP-based electrolyte quickly increased from an initial value of 97.7% to over 99.9% after 20 cycles, and the CE was maintained for over 250 cycles at a practical current density of 2 mA cm^{-2} and an areal capacity of 4 mAh cm^{-2} (Figure 2c,d).

https://doi.org/10.1021/jacs.5c14645
J. Am. Chem. Soc. 2026, 148, 4087−4096

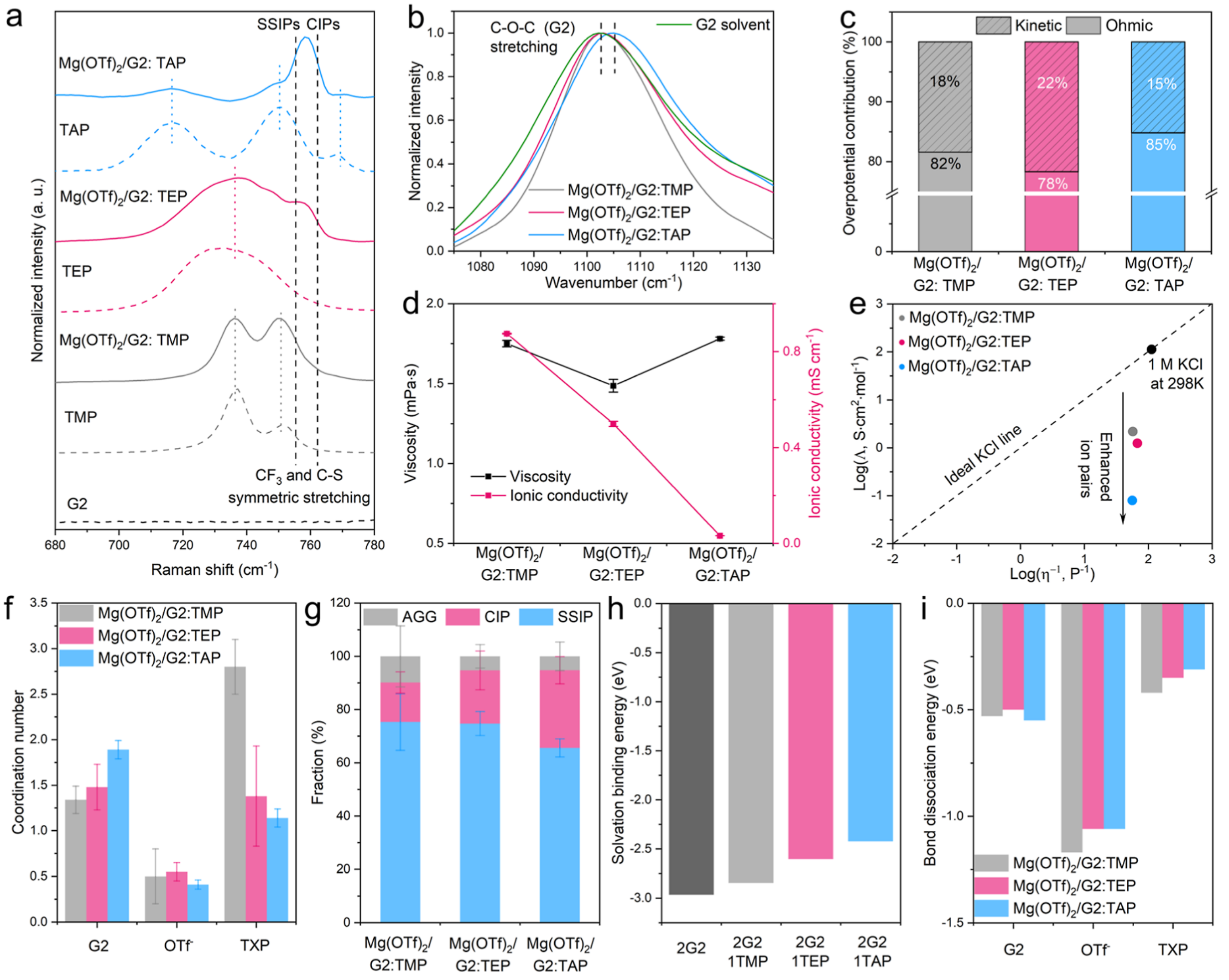

Figure 4. Steric effect-tuned solvation structure. (a) Raman and (b) FTIR spectra of various electrolytes. (c) The estimated ohmic and kinetic overpotential contributions from galvanostatic hold-and-relax measurements of Mg||Mg cells at a low current density of 0.5 mA cm^{-2}. (d) Ionic conductivity and viscosity of various electrolytes at 298 K. (e) The corresponding Walden analysis with viscosity and equivalent ionic conductivity. (f) The coordination number of various solvents and (g) the fractions of aggregates (AGG), CIP, and SSIP in different electrolytes obtained from MD simulations. (h) The DFT-calculated binding energies from Mg^{2+}−2G2 solvation to Mg^{2+}−2G2−1TXP solvation and (i) bond dissociation energy of various solvent molecules coordinated to Mg^+ species.

Comparatively, electrolytes with TMP and TAP only achieved CEs of 96.9% and 94.9% for limited cycles, respectively. The magnesium E/S profiles of asymmetric cells with different electrolytes are shown in Figure 2e−g. In the voltage profiles of the cell using the TMP-based electrolyte, an initial flat plating plateau at an overpotential of ∼490 mV was observed (Figure 2e). However, at the end of the 10th plating process, a second plateau at a higher overpotential of ∼620 mV appeared, contributing ∼1 mAh cm^{-2} capacity. The overpotential of this second plating plateau dramatically increased during the subsequent cycling to more than 3 V after the 30th cycle. This high overpotential continuously increased and finally led to the failure of the plate at 4 mAh cm^{-2}. The appearance of this second plateau at higher overpotentials is due to the consumption of TMP (see below). In contrast, both the TEP and TAP-based electrolytes showed only one plating plateau during the whole measurements (Figure 2f,g), with an overpotential of ∼250 and 740 mV, respectively. This suggests that both TEP and TAP with extended alkyl groups are more stable against decomposition during plating. Furthermore, in contrast to the quick short at the 12th cycle of the TAP electrolyte, the cell employing the TEP electrolyte was stable for more than 250 cycles.

The interfacial stability of magnesium E/S in these electrolytes was further investigated by performing electrochemical impedance spectroscopy (EIS) on Mg||Mg symmetric cells. After an initial activation to remove any electrolyte impurity or native passivation of polished magnesium anodes (Figure S3), the cells were subjected to a constant current density of 1 mA cm^{-2} and an areal capacity of 4 mAh cm^{-2} per cycle (Figure 3a). The EIS measurements were performed after each stripping process. Over the first 10 cycles (80 h), the TEP-based electrolyte showed a stable plating overpotential value of only ∼170 mV (Figure 3b). In the electrolyte using TAP, the initial overpotential was ∼300 mV and slightly decreased to ∼265 mV in the subsequent cycling. However, in the TMP-based electrolyte, a very different overpotential evolution was observed, showing an initial value of ∼300 mV and a quick increase to ~750 mV with a large voltage fluctuation. The representative Nyquist plots for the 10th cycle are shown in Figure 3c. The impedance was fitted by a commonly used equivalent circuit over the first 10 cycles (Figure S4), with a bulk electrolyte resistance (R_{bulk}), interphase resistance (R_{int}) at high frequency, and charge transfer resistance (R_{CT}) at low frequency. The fitted values of the three resistances in the first 10 cycles are depicted in Figure 3d−f. In contrast to the relatively stable and low R_{bulk} in TEP/TAP-based electrolytes (Figure 3d), R_{bulk} in the electrolyte with TMP was much higher, fluctuated heavily, and gradually increased during cycling, indicating decreased electrolyte ionic conductivity due to the progressive TMP decomposition. This matches the increased and fluctuating R_{int} in the TMP-based electrolyte (Figure 3e). These fluctuations in R_{bulk} and R_{int} in the TMP-based electrolyte were consistent with its unstable plating/stripping profile (Figure 2a). R_{CT} in the TEP-based electrolyte was around 70 ohm cm^2 (Figure 3f), more than 3-fold lower than that of the TMP-based electrolyte. It also remained constant during the whole cycling process, consistent with its fast plating/stripping behavior. The initial R_{CT} in the electrolyte with TAP was up to 700 ohm cm^2 before quickly dropping to 220 ohm cm^2, suggesting a possible alteration in the Mg^{2+} solvation sheath that changes the desolvation process. This is probably due to the progressive decomposition of G2 molecules during cycling, resulting in more TAP molecules entering the first solvation structure with enhanced electrochemical stability (see MD/DFT results below). Overall, the facile decomposition of TMP in $Mg(OTf)_2$/G2: TMP, and fast G2 degradation in $Mg(OTf)_2$/G2: TAP induces the highest R_{bulk} and R_{CT}, respectively; whereas in $Mg(OTf)_2$/G2: TEP, both G2 and TEP remain stable, thus showing the lowest R_{bulk} and R_{CT}.

These electrochemical analyses show the vast kinetic difference in magnesium E/S behavior of these electrolytes, originating from the different molecular lengths of the alkyl groups in phosphate solvents. They act to tune the Mg^{2+} solvation sheath via a steric effect and affect the electrolyte decomposition activity to form (SEIs) as discussed below.

Tuning the Mg^{2+} Solvation Sheath by Steric Effects

The steric effect of trialkyl phosphates on the Mg^{2+} solvation structure was revealed by combining multiple spectroscopy studies, molecular dynamics (MD) simulations, and density functional-theory (DFT) calculations. Raman spectroscopy was used to characterize the contact ion pairs (CIPs) in the electrolytes. In the 750−770 cm^{-1} region that corresponds to the CF_3 and C−S symmetric stretch modes, the intensity of the CIPs[19] at 762 cm^{-1} follows the order $Mg(OTf)_2$/G2: TMP < $Mg(OTf)_2$/G2: TEP < $Mg(OTf)_2$/G2: TAP (Figure 4a). An opposite order of the peak intensity at 1033 cm^{-1} corresponds to solvent-separate ion pairs (SSIPs) (Figure S5). Quantitative peak-fitting analysis of the SSIPs and CIPs is not feasible due to the pronounced peak overlap with the TXP signals. This trend matches well with calculated CIP/SSIP fractions in the different electrolytes from the MD simulations (Figure 4g). Fourier-transform infrared spectroscopy (FTIR) was further used to probe the free G2 activity in the electrolytes. In both TMP and TEP-based electrolytes, the wavenumber of the C−O−C stretching mode of G2 remained unchanged relative to that of the pure solvent, in contrast to the significant blue shift to a higher wavenumber in the TAP-based electrolyte (Figure 4b). This was also observed via MD simulations for TMP, TEP, and TAP-based electrolytes, where the coordination number of trialkyl phosphate and G2 decreased from 2.8 and 1.38 to 1.14 and increased from 1.34 and 1.48 to 1.90, respectively (Figure 4f). The coordination number of OTf^- remained relatively similar at 0.5 ± 0.2, 0.55 ± 0.22, and 0.41 ± 0.05 for the TMP, TEP, and TAP-based electrolytes, respectively. This suggests TMP with the lowest steric hindrance has the strongest coordination and hence ability to (mainly) displace G2 from the first solvation shell of the Mg^{2+} ion. However, more G2 enters the Mg^{2+} solvation sheath in the presence of TAP due to TAP's strong steric hindrance and weaker coordination. In contrast, the moderate steric hindrance of TEP results in balanced solvent coordination in the TEP-based electrolyte, where both TEP and G2 exhibit relatively weaker coordination with Mg^{2+}. Such variance in solvent coordination strength results in significant differences in the kinetic overpotential contribution during magnesium E/S. This is confirmed by galvanostatic hold-and-relax measurements where the diffusion overpotential contribution can be considered negligible at a low current density of 0.5 mA cm^{-2} (Figure S6). The estimated kinetic overpotential contributions are 18%, 22%, and 15% in TMP, TEP, and TAP-based electrolytes, respectively, confirming the most facile Mg^{2+} desolvation kinetics in TEP-G2. The poorer desolvation kinetics in TMP and TAP-based electrolytes lead to higher ohmic overpotential contributions of 82% and 85%, respectively.

The above analysis confirms that the ability of trialkyl phosphates to dissociate the Mg^{2+}−G2 interaction and Mg^{2+}−OTf^- ion pairs decreases with increasing alkyl chain length.[20] This is further supported by the same trend in ionic conductivities of the electrolytes at 298 K (Figures 4d and S7): TMP with the shortest chain length has the best capability to dissociate ion pairs, and thus $Mg(OTf)_2$/G2: TMP electrolyte shows the highest ionic conductivity. We note that the TEP-based electrolyte has slightly lower viscosity (Figure 4d), as also verified by MD simulations (Figure S8). This can be ascribed to an optimal solvation structure with balanced G2 and TEP coordination (Figure 4f), in contrast to strong TMP and G2 coordination in TMP and TAP-based electrolytes, respectively. The strong solvent coordination could restrict electrolyte motion and result in higher viscosity.[21] We further performed a Walden analysis that correlates log (equivalent ionic conductivity (Λ)) to the log (1/viscosity (η)), Figure 4e. The diagonal line of the dilute 1 M KCl/H_2O solution ($\log(\Lambda/S\cdot cm^2\cdot mol^{-1}) \approx 2.05$ and $\log(\eta^{-1}/P^{-1}) \approx 2.05$ at 298 K; 1 P = 0.1 $Pa\cdot s^{-1}$), which is considered to be a fully dissociated electrolyte, was used as the reference point.[22−24] All three electrolytes are well below the ideal KCl line, suggesting they are poor ionic conductors[25] due to the significant portion of CIPs relative to the ideal fully dissociated electrolyte. This explains the high contribution of the ohmic resistance to the plating overpotential (Figure 4c). However, compared to the TMP and TEP systems, the TAP-based electrolyte deviates more strongly from the ideal KCl line, which can be ascribed to very poor ion pair dissociation owing to the strong hindrance of bulky TAP. Such a difference in solvent coordination and ion pairing is due to the radius of gyration, a measure of the steric hindrance, which increases with longer alkyl chain length (Table 1). We further used DFT to investigate the solvation binding energy resulting from such a hindrance (Figure 4h). In the absence of TXP, Mg^{2+} is coordinated by 2 G2 molecules with 3 oxygen from each G2 to

Table 1. Most Easily Cleavable Bonds and Radius of Gyration of Various Solvent Molecules Coordinated to a Mg^+ Species[a]

electrolyte species near Mg^+	most easily cleavable bond	radius of gyration (Å)
G2	$-CH_2...O-CH_3$	3.14
OTf^-	$O{=}S...CF_3$	1.67
TMP	$O{=}P-O...CH_3$	1.87
TEP	$O{=}P-O...CH_2-CH_3$	2.45
TAP	$O{=}P-O...CH_2-CH_2-CH_2-CH_2-CH_3$	4.21

[a] See Table S1 for Details.

give a binding energy of −2.97 eV. Upon addition of TXP, one of the oxygens from G2 is pushed out of the first solvation shell of Mg^{2+}, and the oxygen from TXP takes its place. The resultant binding energies for TMP, TEP, and TAP are −2.85 eV, −2.60 eV, and −2.42 eV, giving a solvation energy penalty of 0.12, 0.37, and 0.55 eV, respectively. This shows that as the alkyl length increases, the energy penalty for altering the solvation structure increases due to steric hindrance.

Our earlier DFT studies showed[14,18] that electrolyte decomposition at the Mg/electrolyte interface mainly originates from bond dissociation of anion/solvent near partially reduced Mg^+ species rather than Mg^{2+}. We thus performed further DFT calculations to identify the most easily cleaved bonds in the electrolyte species in the different electrolytes. As summarized in Table 1, in the presence of Mg^+, C−O, C−S, and C−O were identified as the readily cleavable bonds for G2, OTf^-, and TXP (=TMP, TEP, TAP), respectively. The corresponding bond dissociation energies (BDE) are shown in Figure 4i and Table S1. We observed that the direct decomposition of all of the electrolyte species is thermodynamically favorable, where the decomposition of OTf^- is the most thermodynamically favored pathway. It should be noted that in TMP−G2, both TMP and OTf^- have a slightly higher BDE than in TEP or TAP-based electrolytes. In addition, the primary solvation structure of the $Mg(OTf)_2$/G2/TMP electrolyte obtained from MD simulations (Figures S9 and S10) has the most coordinated phosphate solvent and the least coordinated G2 molecules among the three electrolytes. These findings suggest that TMP with the shortest alkyl chain length tends to decompose more progressively than TEP and TAP during cycling, consistent with the EDS and X-ray photoelectron spectroscopy (XPS) results shown below.

Magnesium Deposition Morphologies and Interfacial SEI Chemistry

The magnesium electrodeposition morphologies and formation of the SEI are greatly affected by the solvation structure of Mg^{2+}. The morphology of deposited magnesium was characterized by scanning electron microscopy (SEM) on cycled magnesium metal anodes. In the TMP electrolyte (Figure 5a), needle-shaped magnesium deposits were observed, with some minor porosity. In the TEP electrolyte, hexagonal platelets were evident (Figure 5b) with dimensions of 2−20 μm that crystallize parallel to the substrate and are densely packed without noticeable porosity. Such (0001) textured planar morphology is beneficial for a Mg anode functioning at practical conditions.[26,27] In the TAP electrolyte, smaller hexagonal platelets were observed, which were covered

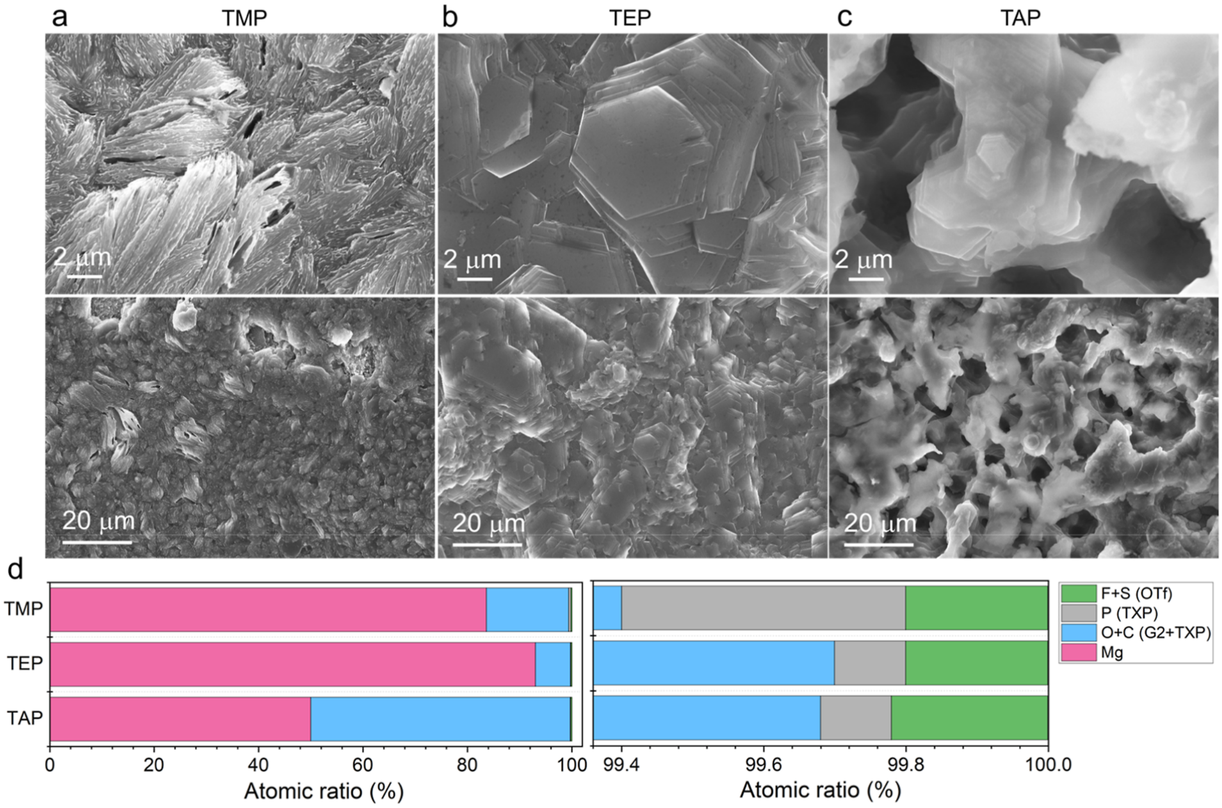

Figure 5. Morphologies of electrodeposited magnesium. SEM images of magnesium anodes cycled in symmetric cells for 30 cycles (after plating) at 0.5 mA cm^{-2} (0.5 mAh cm^{-2}) in 0.2 M $Mg(OTf)_2$ with (a) G2: TMP, (b) G2: TEP, and (c) G2: TAP. (d) The corresponding EDX values of different elements on the surface of deposited magnesium.

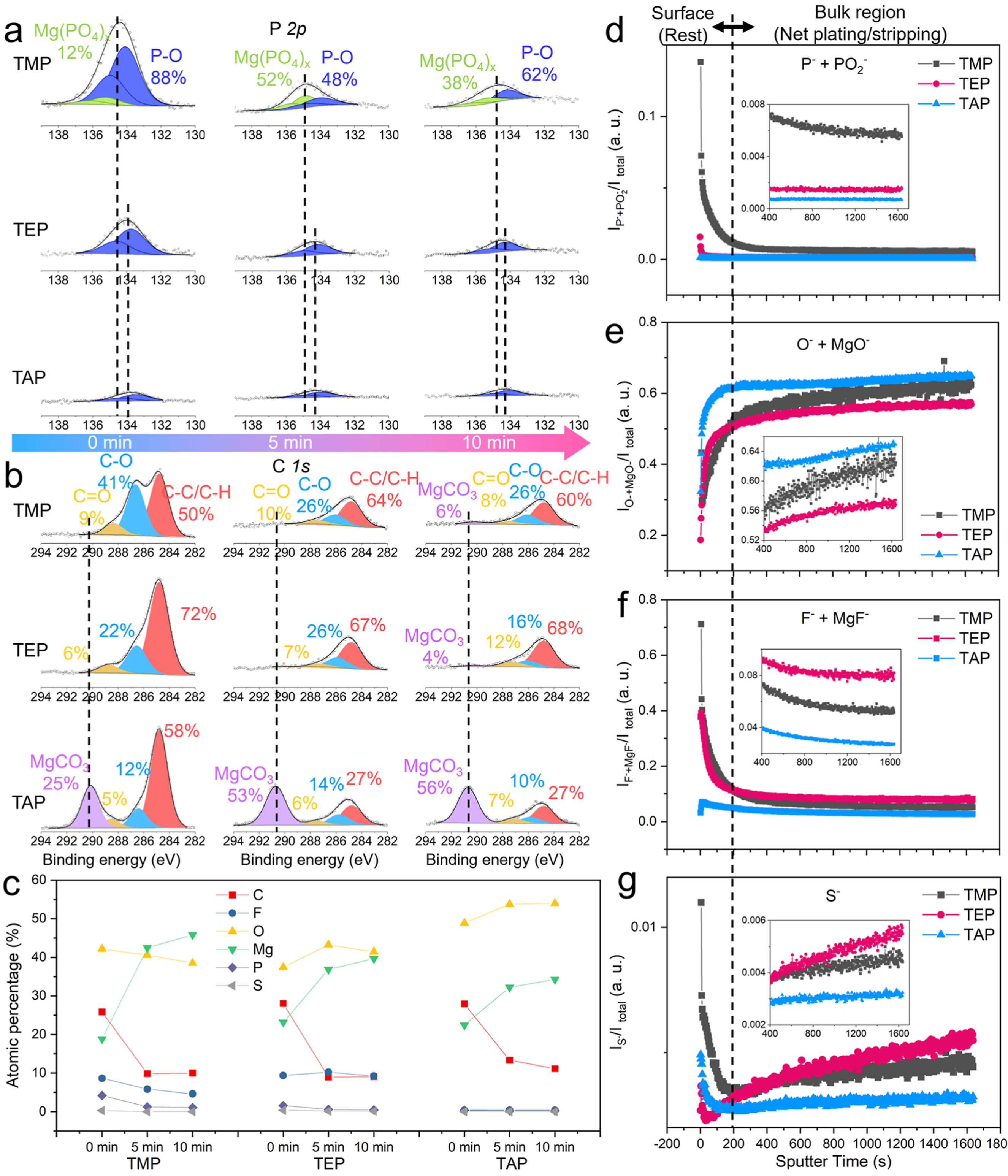

Figure 6. Depth-profiling XPS and ToF-SIMS studies of interfacial solid−electrolyte-interphase chemistry. (a) P *2p*, (b) C *1s* XPS spectra, and (c) corresponding atomic percentages of deposited magnesium in the electrolytes at different sputtering times for 0 min (no sputtering), 5, and 10 min. (d−g) The relative intensities of different ion fragments as a function of sputter time obtained from ToF-SIMS: (d) P^- + PO^{2-} from TXP solvents, (e) O^- + MgO^- from both TXP and G2 solvents, (f) F^- + MgF^- and (g) S^- from OTf^- anions. The intensities of all ion fragments quickly drop in the initial 200 s sputtering, corresponding to reactions at the freshly deposited Mg/electrolyte interface during the rest period; the subsequent stable-intensity region refers to the SEI formed in the bulk region of deposited Mg during the net plating process. All Mg anodes were collected from Mg||Mg cells after 20 cycles at 0.5 mA cm^{-2} and 0.5 mAh cm^{-2}.

with insulating species and large holes and vacancies (Figure 5c). The element distribution on the surface of deposited magnesium was determined by energy-dispersive X-ray spectroscopy (EDX, Figure 5d). Significantly higher phosphorus

https://doi.org/10.1021/jacs.5c14645
J. Am. Chem. Soc. 2026, 148, 4087−4096

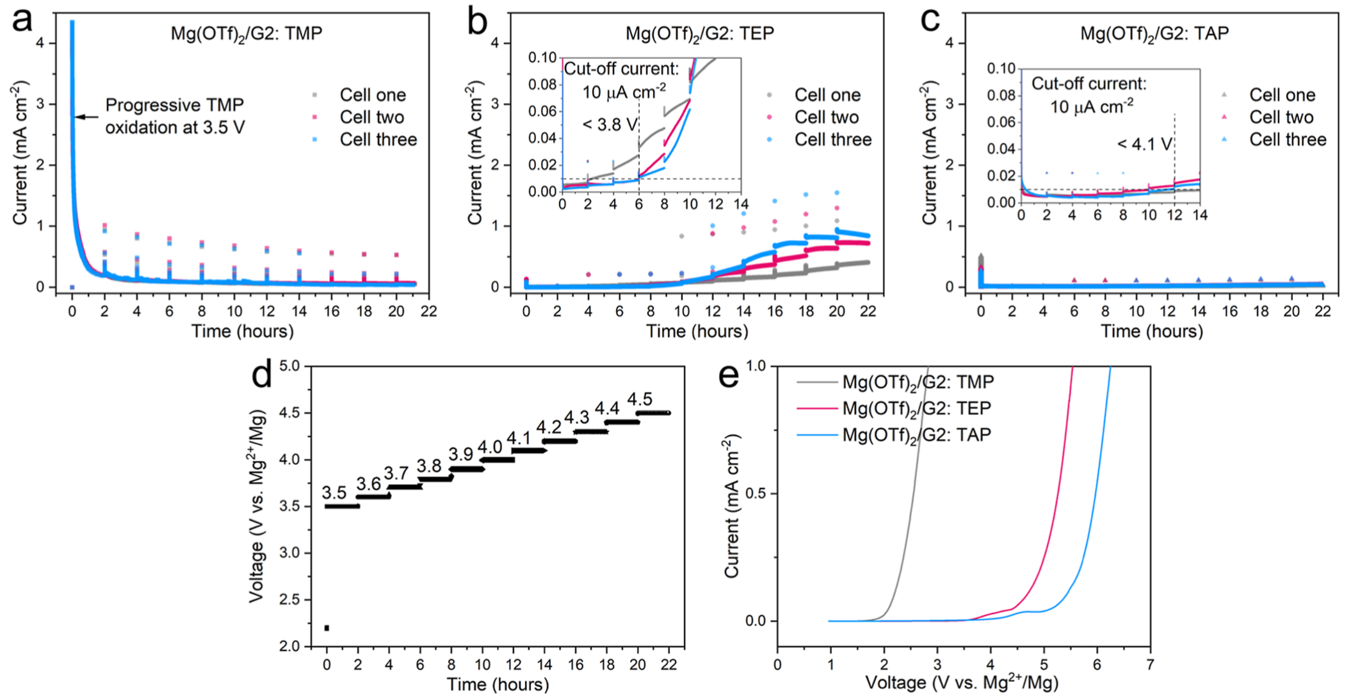

Figure 7. Steric effect of trialkyl phosphates on the oxidative stability of different electrolytes on Pt current collectors. (a−c) The leakage-current response from potential-hold measurements at various fixed anodic potentials from 3.5 to 4 V in (a) Mg(OTf)$_2$/G2: TMP, (b) Mg(OTf)$_2$/G2: TEP, (c) Mg(OTf)$_2$/G2: TAP, and (d) the corresponding voltage profiles. (e) The leakage-current response from LSV measurements in the different electrolytes as labeled. Pt foil was used as the working electrode, and Mg foil as both counter and reference electrodes.

signals were seen for magnesium deposited in the TMP electrolyte compared to those in the TEP or TAP electrolyte. This indicates that the decomposition of TMP might be the origin of the absence of hexagonal morphology. In addition, much higher carbon and oxygen content was observed for magnesium deposited in the TAP electrolyte, suggesting progressive G2 decomposition that could be ascribed to the more coordinated G2 in the solvation structure,[15] consistent with the FTIR analysis (Figure 4b).

The electrolyte decomposition during plating results in complex SEI compositions on the magnesium surface, as investigated by depth-profiling XPS. In the P 2*p* spectra of magnesium deposited in both TEP and TAP-based electrolytes, the surface showed P−O signals that originate from the adsorption of phosphate solvents (Figure 6a). In contrast, in the TMP-based electrolyte, this feature showed a significant increase in intensity and a shift to a higher binding energy, which was ascribed to an extra $Mg(PO_4)_x$ component. The decomposition of TMP to $Mg(PO_4)_x$ during magnesium plating is consistent with the behavior of a previously reported electrolyte (0.5 M $Mg(TFSI)_2$/DME/TMP (~10:1 in vol)).[28] After Ar^+ sputtering for 5 or 10 min, the P 2*p* signals on the deposited magnesium in all three electrolytes decreased in intensity. In the C 1*s* spectra (Figure 6b), the surface of the magnesium in the TMP and TEP electrolytes showed similar fractions of adventitious carbon, including C−C/C−H, C−O, and C═O components. However, in the TAP electrolyte, an additional signal at 290.1−290.4 eV was observed, which was attributed to $MgCO_3$ resulting from the decomposition of G2.[6,12] After sputtering for 10 min, only negligible $MgCO_3$ remained on magnesium deposited in the TMP and TEP electrolytes, in contrast to its dominance in the TAP electrolyte. The presence of such a thick $MgCO_3$-rich SEI was also confirmed in Mg 2*p* spectra (Figure S11), where no Mg^0 species could be observed on the magnesium surface. Figure 6c and Table S2 summarize the atomic percentages from XPS analysis: phosphorus follows the order of TMP > TEP > TAP, suggesting effectively higher TMP decomposition in the TMP-based electrolyte; whereas oxygen follows the order of TMP ≈ TEP < TAP, indicating significantly higher G2 decomposition in the TAP-based electrolyte. We thus ascribe the copious presence of $MgCO_3$ to the strong G2 coordination (Figure 4a,f) in the first solvation shell of Mg^{2+} in the TAP-based electrolyte (Figure 4a), thus inducing its easy decomposition.[6,15,28] These G2-derived decomposition species quickly passivate the Mg surface and block electron transfer for further anion decomposition to form MgF_2 and MgS (Figures S12 and S13).

We further used depth-profiling time-of-flight secondary ion mass spectrometry (ToF-SIMS) to investigate the SEI evolution from the surface to the bulk of the deposited magnesium. As shown in Figures 6d−g and S14, all ion fragments either increase or decrease rapidly in the initial 200 s and become stable after subsequent sputtering time. We thus correlate these two regions to the surface and bulk of the deposited magnesium. The anion/solvent adsorption and their chemical reaction with freshly deposited magnesium during the rest period could lead to a much higher intensity on the surface relative to the bulk region. Therefore, the observed ion fragment evolution as a function of sputter time reflects the interfacial chemistry during cell rest and net plating/stripping, respectively. We observe much higher P^- and PO_2^- fragments on the surface and in the bulk region of magnesium cycled in TMP−G2 (Figure 6d), consistent with the XPS analysis suggesting continuous TMP decomposition. Higher levels of O^- and MgO^- fragments are observed for magnesium collected from TAP−G2 (Figure 6e), confirming progressive G2 decomposition. In addition, the O^-/MgO^- ion fragments are more intense in the bulk than on the surface, suggesting that G2 decomposition occurs during plating/stripping. This aligns with a previous computational study that shows G2 reduces when it accepts an electron at the magnesium/electrolyte interface.[15] As a consequence, the TAP-based electrolyte with the most coordinated G2 (Figure 4a,f) shows the greatest G2 decomposition. All three electrolytes exhibit a low intensity of anion-related ion fragments (F^-, MgF^-, and S^-) in the bulk region. This implies anion decomposition is suppressed by these polar TXP solvents during magnesium E/S, whereas on the surface, much higher F/S-related signals are observed. These findings are in perfect accord with our previous report, which showed that an almost bare F/S-rich interface exists in the bulk during dynamic plating/stripping,[18] while a thin anion-derived SEI exists on the top surface due to the chemical reaction between the electrolyte and freshly deposited magnesium.

We finally evaluate the effect of steric hindrance of the trialkyl phosphates on the oxidative stability of these electrolytes using a Pt foil as the working electrode and magnesium foil as both counter and reference electrodes. The potential-hold leakage-current measurements (Figure 7a−d) show both TEP and TAP-based electrolytes have high oxidative stability up to 3.8 and 4.1 V, respectively. However, TMP-G2 shows progressive electrolyte decomposition from the start, indicating its poor oxidative stability that lies well below 3.5 V. The lower leakage current responses at subsequent higher potentials are due to the depletion of the TMP solvent. Such poor oxidative stability is confirmed by linear scan voltammetry (LSV) measurements (Figure 7e), showing an onset oxidation potential at ∼2 V in TMP-G2, in contrast to ∼4 V in the TEP/TAP-based electrolytes. Furthermore, TAP-G2 also shows a lower current response than TEP-G2 in both potential-hold and LSV measurements, confirming the increased electrochemical stability of TAP due to more steric hindrance.

■ CONCLUSIONS

In this work, we symmetrically studied the bulk and interfacial electrochemistry of the trialkyl phosphate−G2 cosolvent in $Mg(OTf)_2$-based chloride-free electrolytes. Our results show the vital importance of the alkyl chain length of these phosphates in determining the solvent stability against interfacial electrochemical decomposition at the Mg/electrolyte interface and the capability to dissociate (or "dissolve") Mg^{2+}−triflate/G2. We attribute these variances to the steric hindrance due to different alkyl chain lengths that results in a significant difference in the radius of gyration. These alter the Mg^{2+} solvation sheath that ultimately changes the electrolyte decomposition pathway to various solvent-derived species and very distinctive SEIs. Our work demonstrates one critical aspect in designing Mg^{2+} ion electrolytes, that changing one chemical group on one solvent molecule can lead to vastly different electrochemistry. This opens up wide opportunities in designing chloride-free Mg^{2+} electrolytes as well as other nonaqueous metal ion (Li^+, Na^+, and Ca^{2+}) electrolytes.

■ ASSOCIATED CONTENT

Data Availability Statement

The data supporting the findings of this study are available within the Article and its Supporting Information or from the authors.

Supporting Information

The Supporting Information is available free of charge at https://pubs.acs.org/doi/10.1021/jacs.5c14645.

Experimental details, additional electrochemical performances, characterization data, and computational results of trialkyl phosphate-based electrolytes (PDF)

■ AUTHOR INFORMATION

Corresponding Author

Linda F. Nazar − *Department of Chemistry and the Waterloo Institute for Nanotechnology, University of Waterloo, Waterloo, Ontario N2L 3G1, Canada; Joint Center for Energy Storage Research, Argonne National Laboratory, Lemont, Illinois 60439, United States;* orcid.org/0000-0002-3314-8197; Email: lfnazar@uwaterloo.ca

Authors

Chang Li − *Department of Chemistry and the Waterloo Institute for Nanotechnology, University of Waterloo, Waterloo, Ontario N2L 3G1, Canada; Joint Center for Energy Storage Research, Argonne National Laboratory, Lemont, Illinois 60439, United States*

Rohith Srinivaas Mohanakrishnan − *Department of Materials Science and Engineering, UC Berkeley, Berkeley, California 94720, United States;* orcid.org/0000-0003-1898-0660

Jinghan Li − *Department of Chemistry and the Waterloo Institute for Nanotechnology, University of Waterloo, Waterloo, Ontario N2L 3G1, Canada; Joint Center for Energy Storage Research, Argonne National Laboratory, Lemont, Illinois 60439, United States*

Rishabh D. Guha − *Materials Science Division, Lawrence Berkeley National Laboratory, Berkeley, California 94720, United States;* orcid.org/0000-0003-1977-6039

Kristin A. Persson − *Department of Materials Science and Engineering, UC Berkeley, Berkeley, California 94720, United States; Materials Science Division, Lawrence Berkeley National Laboratory, Berkeley, California 94720, United States*

Complete contact information is available at: https://pubs.acs.org/10.1021/jacs.5c14645

Notes

The authors declare no competing financial interest.

■ ACKNOWLEDGMENTS

This work was supported by NSERC through funds to L.F.N. via the Discovery Grant and Canada Research Chair programs. K.A.P. and R.S.M. were financed by the U.S. Department of Energy, Office of Science, Office of Basic Energy Sciences, Materials Sciences and Engineering Division, under contract no. DE-AC02-05-CH11231 (D2S2 programme, KCD2S2). R.G. gratefully acknowledges the Moore Foundation Grant, which is funded by the Gordon and Betty Moore Foundation, under Grant no. 10454.

■ REFERENCES

(1) Trahey, L.; Brushett, F. R.; Balsara, N. P.; Ceder, G.; Cheng, L.; Chiang, Y.; Hahn, N.; Ingram, B. J.; Minteer, S. D.; Moore, J. S.; Mueller, K. T.; Nazar, L. F.; Persson, K. A.; Siegel, D. J.; Xu, K.; Zavadil, K. R.; Srinivasan, V.; Crabtree, G. W. Energy storage

emerging: A perspective from the Joint Center for Energy Storage Research. *PANS* **2020**, *117*, 12550−12557.

(2) Mohtadi, R.; Tutusaus, O.; Arthur, T. S.; Zhao-Karger, Z.; Fichtner, M. The metamorphosis of rechargeable magnesium batteries. *Joule* **2021**, *5*, 581−617.

(3) Yoo, H. D.; Shterenberg, I.; Gofer, Y.; Gershinsky, G.; Pour, N.; Aurbach, D. Mg rechargeable batteries: an on-going challenge. *Energy Environ. Sci.* **2013**, *6*, 2265−2279.

(4) Aurbach, D.; Lu, Z.; Schechter, A.; Gofer, Y.; Gizbar, H.; Turgeman, R.; Cohen, Y.; Moshkovich, M.; Levi, E. Prototype systems for rechargeable magnesium batteries. *Nature* **2000**, *407*, 724−727.

(5) Wen, T.; Deng, Y.; Qu, B.; Huang, G.; Song, J.; Xu, C.; Du, A.; Xie, Q.; Wang, J.; Cui, G.; Peng, D.; Zhou, X.; Pan, F. Re-envisioning the key factors of magnesium metal anodes for rechargeable magnesium batteries. *ACS Energy Lett.* **2023**, *8* (11), 4848−4861.

(6) Hou, S.; Ji, X.; Gaskell, K.; Wang, P.; Wang, L.; Xu, J.; Sun, R.; Borodin, O.; Wang, C. Solvation sheath reorganization enables divalent metal batteries with fast interfacial charge transfer kinetics. *Science* **2021**, *374* (6564), 172−178.

(7) Blázquez, J. A.; Maça, R. R.; Leonet, O.; Azaceta, E.; Mukherjee, A.; Zhao-Karger, Z.; Li, Z.; Kovalevsky, A.; Fernández-Barquín, A.; Mainar, A. R.; Jankowski, P.; Rademacher, L.; Dey, S.; Dutton, S. E.; Grey, C. P.; Drews, J.; Häcker, J.; Danner, T.; Latz, A.; Sotta, D.; Palacin, M. R.; Martin, J.; Lastra, J. M. G.; Fichtner, M.; Kundu, S.; Kraytsberg, A.; Ein-Eli, Y.; Noked, M.; Aurbach, D. A practical perspective on the potential of rechargeable Mg batteries. *Energy Environ. Sci.* **2023**, *16*, 1964−1981.

(8) Tutusaus, O.; Mohtadi, R.; Arthur, T. S.; Mizuno, F.; Nelson, E. G.; Sevryugina, Y. V. An efficient halogen-free electrolyte for use in rechargeable magnesium batteries. *Angew. Chem., Int. Ed.* **2015**, *54*, 7900−7904.

(9) Dong, H.; Tutusaus, O.; Liang, Y.; Zhang, Y.; Lebens-Higgins, Z.; Yang, W.; Mohtadi, R.; Yao, Y. High-power Mg batteries enabled by heterogeneous enolization redox chemistry and weakly coordinating electrolytes. *Nat. Energy* **2020**, *5*, 1043−1050.

(10) Li, C.; Shyamsunder, A.; Key, B.; Yu, Z.; Nazar, L. F. Stabilizing magnesium plating by a low-cost inorganic surface membrane for high-voltage and high-power Mg batteries. *Joule* **2023**, *7*, 2798−2813.

(11) Li, C.; Guha, R. D.; Shyamsunder, A.; Persson, K. A.; Nazar, L. F. A weakly ion pairing electrolyte designed for high voltage magnesium batteries. *Energy Environ. Sci.* **2024**, *17*, 190−201.

(12) Sun, Y.; Wang, Y.; Jiang, L.; Dong, D.; Wang, W.; Fan, J.; Lu, Y. Non-nucleophilic electrolyte with non-fluorinated hybrid solvents for long-life magnesium metal batteries. *Energy Environ. Sci.* **2023**, *16*, 265−274.

(13) Liang, Y.; Dong, H.; Aurbach, D.; Yao, Y. Current status and future directions of multivalent metal-ion batteries. *Nat. Energy* **2020**, *5*, 646−656.

(14) Rajput, N. N.; Qu, X.; Sa, N.; Burrell, A. K.; Persson, K. A. The Coupling between Stability and Ion Pair Formation in Magnesium Electrolytes from First-Principles Quantum Mechanics and Classical Molecular Dynamics. *J. Am. Chem. Soc.* **2015**, *137*, 3411−3420.

(15) Baskin, A.; Prendergast, D. Exploration of the Detailed Conditions for Reductive Stability of Mg(TFSI)$_2$ in Diglyme: Implications for Multivalent Electrolytes. *J. Phys. Chem. C* **2016**, *120*, 3583−3594.

(16) Huang, X.; Tan, S.; Chen, J.; Que, Z.; Deng, R.; Long, J.; Xiong, F.; Huang, G.; Zhou, X.; Li, L.; Wang, J.; Mai, L.; Pan, F. Asymmetric $SO_3CF_3^-$-Grafted Boron-Center Anion Enables Boron-Containing Interphase for High-Performance Rechargeable Mg Batteries. *Adv. Funct. Mater.* **2024**, *34* (17), 2314146.

(17) Zhang, D.; Wang, Y.; Yang, Y.; Zhang, Y.; Zhao, Y.; Pan, M.; Sun, Y.; Chen, S.; Liu, X.; Wang, J.; et al. NuLi. Constructing Efficient $Mg(CF_3SO_3)_2$ Electrolyte via Tailoring Solvation and Interface Chemistry for High-Performance Rechargeable Magnesium Batteries. *Adv. Energy Mater.* **2023**, *13* (39), 2301795.

(18) Li, C.; Guha, R. D.; House, S. D.; Bazak, J. D.; Yu, Y.; Zhou, L.; Zavadil, K.; Persson, K. A.; Nazar, L. F. A dynamically bare metal interface enables reversible magnesium electrodeposition at 50 mAh cm^{-2}. *Joule* **2025**, *9* (2), 101790.

(19) Nguyen, D. T.; Eng, A. Y. S.; Ng, M.; Kumar, V.; Sofer, Z.; Handoko, A. D.; Subramanian, G. S.; Seh, Z. W. A High-Performance Magnesium Triflate-based Electrolyte for Rechargeable Magnesium Batteries. *Cell Rep. Phys. Sci.* **2020**, *1* (12), 100265.

(20) Chen, Y.; Yu, Z.; Rudnicki, P.; Gong, H.; Huang, Z.; Kim, S. C.; Lai, J.; Kong, X.; Qin, J.; Cui, Y.; Bao, Z. Steric Effect Tuned Ion Solvation Enabling Stable Cycling of High-Voltage Lithium Metal Battery. *J. Am. Chem. Soc.* **2021**, *143* (44), 18703−18713.

(21) Yao, N.; Yu, L.; Fu, Z.; Shen, X.; Hou, T.; Liu, X.; Gao, Y.; Zhang, R.; Zhao, C.; Chen, X.; Zhang, Q. Probing the Origin of Viscosity of Liquid Electrolytes for Lithium Batteries. *Angew. Chem., Int. Ed.* **2023**, *62*, No. e202305331.

(22) Mariani, A.; Bonomo, M.; Gao, X.; Centrella, B.; Nucara, A.; Buscaino, R.; Barge, A.; Barbero, N.; Gontrani, L.; Passerini, S. The unseen evidence of Reduced Ionicity: The elephant in (the) room temperature ionic liquids. *J. Mol. Liq.* **2021**, *324*, 115069.

(23) Schreiner, C.; Zugmann, S.; Hartl, R.; Gores, H. J. Fractional Walden Rule for Ionic Liquids: Examples from Recent Measurements and a Critique of the So-Called Ideal KCl Line for the Walden Plot. *J. Chem. Eng. Data* **2010**, *55*, 1784−1788.

(24) MacFarlane, D. R.; Forsyth, M.; Izgorodina, E. I.; Abbott, A. P.; Annat, G.; Fraser, K. On the concept of ionicity in ionic liquids. *Phys. Chem. Chem. Phys.* **2009**, *11*, 4962−4967.

(25) Ellison, J. H. J.; Grey, C. P. Engineering considerations for practical lithium−air electrolytes. *Faraday Discuss.* **2024**, *248*, 355.

(26) Wang, G.; Liu, X.; Shi, H.; Ma, Y.; Wang, Z.; Sun, C.; Song, F.; Zhang, Z.; Dong, S.; Sun, M.; Du, A.; Cui, G. Achieving Planar Electroplating/Stripping Behavior of Magnesium Metal Anode for a Practical Magnesium Battery. *ACS Energy Lett.* **2024**, *9*, 48−55.

(27) Yang, G.; Li, Y.; Wang, J.; Lum, Y.; Lim, C. Y. J.; Ng, M.; Zhang, C.; Chang, Z.; Zhang, Z.; Handoko, A. D.; Ghosh, T.; Li, S.; Sofer, Z.; Liu, W.; Yao, Y.; Seh, Z. W. Realizing horizontal magnesium platelet deposition and suppressed surface passivation for high-performance magnesium metal batteries. *Energy Environ. Sci.* **2024**, *17*, 1141−1152.

(28) Zhao, W.; Pan, Z.; Zhang, Y.; Liu, Y.; Dou, H.; Shi, Y.; Zuo, Z.; Zhang, B.; Chen, J.; Zhao, X.; Yang, X. Tailoring Coordination in Conventional Ether-based Electrolytes for Reversible Magnesium Metal Anodes. *Angewandte Chemie* **2022**, *134* (30), No. e202205187.